Nano Research

Open Access

Research Article

Broadband microwave absorption and all-weather anti-solid fouling enabled by a self-lubricating rGO@Fe_3O_4 composite

Huaiyu Dong[1,§], Tongtong Hao[2,§], Yixin Chen[3,4], Yixing Huang[1] ✉, Jing Wang[3,4] ✉, and Zhiyuan He[2] ✉

[1] *Beijing Key Laboratory of Advanced Metamaterial Structures and Functional Technologies, Institute of Advanced Structure Technology, Beijing Institute of Technology, Beijing 100081, China*
[2] *School of Materials Science and Engineering, Beijing Institute of Technology, Beijing 100081, China*
[3] *School of Mechanical Engineering, Shanghai Jiao Tong University, Shanghai 200240, China*
[4] *State Key Laboratory of Mechanical Systems and Vibration, Shanghai Jiao Tong University, Shanghai 200240, China*
[§] *Huaiyu Dong and Tongtong Hao contributed equally to this work.*

Cite this article: *Nano Research*, **2026**, *19*, 94908933. https://doi.org/10.26599/NR.2026.94908933

ABSTRACT: The integration of efficient anti-solid fouling and high-performance microwave absorption into a single material platform remains a critical challenge, limiting advancements in radar stealth, aerospace, and Arctic infrastructures. Herein, we present a self-lubricating composite with embedded hydroxylated Fe_3O_4-reduced graphene oxide (rGO@Fe_3O_4) hybrids that overcomes this challenge through a synergistic hierarchical architecture. This composite exhibits unprecedented multifunctionality: simultaneous anti-fouling and de-icing, self-healing, exceptional low-temperature adaptability (down to −60 °C), and ultra-broadband microwave absorption. Leveraging the synergistic design of dielectric and magnetic losses, the composite achieves an effective absorption bandwidth of 6.6 GHz and a minimum reflection loss of −41.3 dB. Radar cross-section measurements reveal an average reduction of 8.15 and 5.5 dB under vertical and horizontal polarizations, respectively. Furthermore, the incorporation of rGO@Fe_3O_4 significantly enhances the composite's adhesive strength across various substrates. Notably, the incorporation of a dynamically regenerating paraffin lubrication phase does not compromise microwave absorption, resolving a long-standing trade-off between anti-solid fouling and electromagnetic impedance matching. This synergistic coupling enables stable broadband absorption performance even under repeated fouling, de-icing, and lubrication-regeneration cycles. These findings highlight the multifunctional composite's potential for practical applications in all-weather anti-solid adhesion and radar stealth, paving a new pathway for advanced surface engineering.

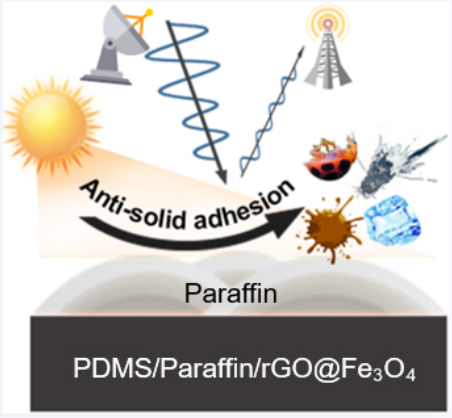

KEYWORDS: solid repellency, microwave absorption, composite materials, self-lubricating, anti/de-icing

1 Introduction

Solid fouling—defined as the undesired adhesion of solid substances such as ice, dust, salt, or biological residues onto material surfaces—is a pervasive challenge in both civilian and military applications. It can severely degrade the surface properties and functionalities of various materials, leading to performance loss, shortened service life, and increased maintenance costs [1–3]. Particularly in electromagnetic absorbing materials, which are often deployed in harsh outdoor service environments, solid fouling poses a serious threat by altering surface impedance, increasing backscattering, and compromising stealth performance (Figs. 1(a) and 1(b)). Therefore, enabling solid repellency on electromagnetic absorbing materials is critical for ensuring their long-term performance [4, 5]. Solid fouling can take diverse forms depending on the environment: icing in low-temperature and high-humidity regions, dust accumulation in desert and dry zones, and salt deposition in marine atmospheres. Each type of foulant has its unique modulus and adhesion strength (Fig. 1(c)), but all share common consequences: increased surface roughness, reduced energy efficiency, and failure of stealth or thermal management systems [6–8]. Current surface-engineering approaches often repel

Received: March 29, 2026; **Revised:** June 11, 2026
Accepted: June 15, 2026

✉Address correspondence to Yixing Huang, huangyixingcurious@163.com; Jing Wang, juw6@sjtu.edu.cn; Zhiyuan He, hezy@bit.edu.cn

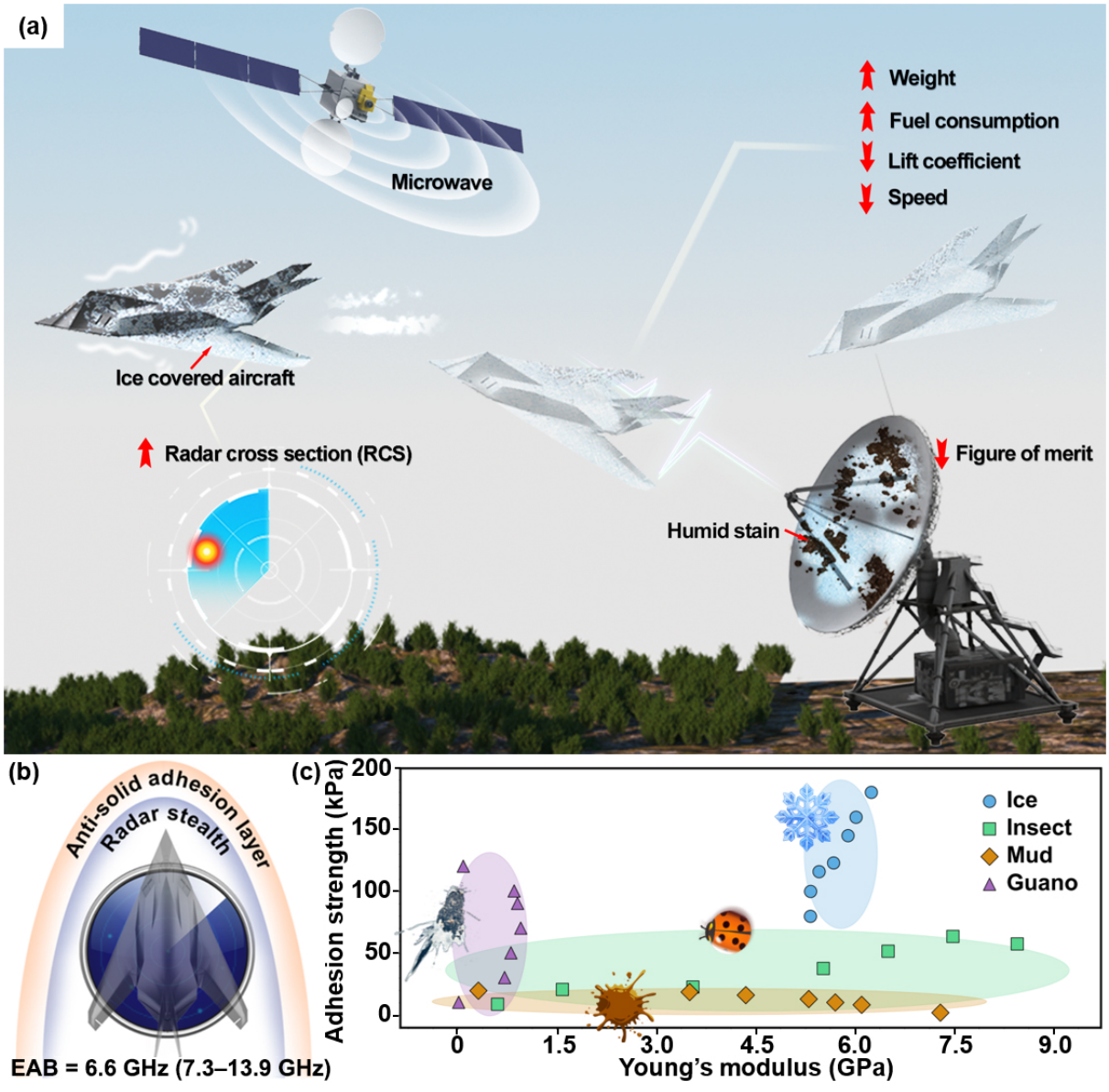

Figure 1 Design rationale and implementation conditions of the multifunctional coating. (a) The adverse impact of humid stain accumulation on aircraft and antennas. (b) Design principle of anti-solid adhesion and radar stealth. (c) Distribution map of Young's modulus and adhesion strength of typical solid contaminants.

a single foulant type, lacking generalizable strategies for combating multiple fouling modes in a single material system.

For example, anti/de-icing methods usually involve creating a solid–air composite interface to reduce the contact area of ice, that is, superhydrophobic surfaces (contact angle ≥ 150°) [9–12]. Such superhydrophobic surfaces can exhibit excellent de-icing performance, particularly combined with electrothermal or photothermal functionalities. However, superhydrophobic surfaces cannot survive and provide anti-fouling performance under bacterial solution or seawater, limiting their repellency to some specific foulants. Another recent anti-fouling material is the fluid-infused lubricating surfaces, which offer improved pressure stability [13–15]. These surfaces reduce adhesion strength for a wide range of solids, including ice, frost, and biological materials, and can passively enable removal by gravity or ambient wind [16]. However, these surfaces are prone to mechanical wear, fluid shear, and high vaporization conditions. They often lack durability in cyclic anti/de-icing scenarios. Therefore, improving the mechanical durability and self-healing capabilities of such surfaces under operational wear is another key unsolved problem. More importantly, the growing demand for multifunctional materials in aerospace and defense applications has stimulated extensive efforts to integrate electromagnetic wave absorption with environmental adaptability. Previous studies have demonstrated partial integrations, such as hydrophobic radar-absorbing coatings or infrared–radar dual-stealth materials [17, 18]. However, the simultaneous realization of broadband microwave absorption and robust anti-solid fouling remains largely unexplored. This challenge arises from an intrinsic materials dilemma: surface lubrication or liquid-infused strategies, while highly effective for reducing solid adhesion, are generally considered detrimental to electromagnetic impedance matching and wave attenuation [19–22].

Herein, we address this long-standing trade-off by proposing a microwave-absorptive anti-solid-adhesion (MASA) composite that integrates hydroxylated Fe_3O_4 nanoparticles and reduced graphene oxide (rGO) within a PDMS matrix, coupled with a dynamically

regenerating paraffin lubrication phase. Rather than treating anti-fouling and microwave absorption as independent functionalities, this work demonstrates a synergistic hierarchical architecture in which the rGO@Fe_3O_4 network governs dielectric and magnetic losses, while the paraffin phase enables adaptive surface lubrication without compromising electromagnetic performance. Notably, the introduction of a mobile liquid phase is conventionally avoided in microwave absorbers due to concerns over impedance mismatch and absorption degradation. In contrast, this study reveals that a carefully engineered rGO@Fe_3O_4 conductive–magnetic network can stabilize impedance matching and sustain broadband absorption even under repeated lubrication–regeneration cycles. As a result, the MASA composite simultaneously achieves ultra-broadband microwave absorption, low ice and contaminant adhesion, self-healing lubrication, and mechanical robustness across extreme environmental conditions. This work establishes a new coupling paradigm for multifunctional composites, providing a viable pathway for all-weather stealth and anti-fouling surface engineering.

2 Experimental section

2.1 Materials

The chemical reagents used in this experiment included sodium hydroxide (NaOH, 96%), triethanolamine (TEA, 99%), ferric chloride hexahydrate ($FeCl_3{\cdot}6H_2O$, 99%), ferrous chloride tetrahydrate ($FeCl_2{\cdot}4H_2O$, 99%), liquid paraffin, polydimethylsiloxane (PDMS), and bisphenol A diglycidyl ether. All reagents were purchased from Aladdin Biochemical Technology Co., Ltd. (Shanghai, China). rGO (carbon content 65%) was obtained from Macklin Biochemical Technology Co., Ltd. (Shanghai, China). All chemicals were of analytical grade and used without further purification.

2.2 Synthesis of Fe_3O_4 nanoparticles

First, 405 mL of ethylene glycol and 135 mL of deionized water were mixed. Subsequently, 25.92 g of sodium hydroxide, 16.2 g of triethanolamine, and 17.514 g of ferric chloride hexahydrate were added to the solution under magnetic stirring until completely dissolved, forming a brownish-yellow transparent solution. A separate batch of the solution was prepared using the same solvent compositions, in which 25.92 g of sodium hydroxide, 16.2 g of triethanolamine, and 8.586 g of ferrous chloride tetrahydrate were added under identical stirring conditions, resulting in a greenish transparent solution. These two solutions were mixed under stirring to form a colloidal suspension. The resulting mixture was transferred to a Teflon-lined autoclave and subjected to hydrothermal treatment at 110 °C for 20 h. After completion of the reaction, the autoclave was allowed to cool naturally to room temperature, and the resulting black precipitate was collected. The precipitate was washed repeatedly with deionized water and dried at 70–75 °C to produce hydroxyl-rich black Fe_3O_4 nanoparticles. The synthetic route is depicted in Fig. S1 in the Electronic Supplementary Material (ESM).

2.3 Preparation of PDMS/Paraffin/rGO@Fe_3O_4 composites

A composite film was prepared using the following weight ratios: PDMS (80 wt.%), liquid paraffin (10 wt.%), rGO (2.5 wt.%), and Fe_3O_4 nanoparticles (7.5 wt.%). The weight ratio of PDMS refers to the combined weight of its base and curing agent in a 10:1 ratio. Initially, rGO and Fe_3O_4 nanoparticles were dispersed in 100 mL of deionized water and subjected to ultrasonication for 30 min. The mixture was dried at 70 °C to obtain rGO@Fe_3O_4 composite powder. This powder was added to PDMS and manually stirred for five minutes. Liquid paraffin was subsequently introduced, and the mixture was further stirred for three minutes until homogeneity was achieved. The resulting black colloidal mixture was poured into pre-prepared molds, degassed under vacuum for two hours, and subsequently cured in an oven at 80 °C for 4 h to obtain the black composite film, designated as MASA. Films with varying rGO-to-Fe_3O_4 ratios were prepared. The detailed compositions of these films are listed in Tables S1 and S2 in the ESM.

2.4 Characterizations

The crystal structures of Fe_3O_4 nanoparticles and rGO@Fe_3O_4 composites were analyzed using X-ray diffraction (XRD, Bruker D8 Advance, Germany). Field-emission scanning electron microscopy (SEM, ZEISS sigma500, Germany), supplemented by energy-dispersive X-ray spectroscopy (EDS, BRUKER XFlash 6130), was employed to examine the microstructure and elemental composition analysis. Transmission electron microscopy (TEM, Hitachi HT7700, Japan) was used to investigate the internal fine structures. X-ray photoelectron spectroscopy (XPS, ThermoFisher Nexsa, USA) was utilized to determine surface elemental composition and chemical states. The distribution and regeneration of liquid paraffin on the composite film were observed using an optical microscope (W2-AF850, Shenzhen Auswei Optical Instruments, China). Wettability of the composite film before and after de-icing was measured with a contact angle goniometer (SZ-CAMC33, China). A thermal imaging camera (Fluke Ti480 PRO 60Hz, USA) recorded temperature changes under simulated solar irradiation to evaluate photothermal conversion performance. An adhesion strength testing device was set up to measure the ice adhesion strength and the adhesion behavior on various substrates (Fig. S22 in the ESM). A solar simulator (CEL-AAAS50, Beijing, China Education Golden Source Technology Co., Ltd., China) was used to evaluate the de-icing and phase transition behavior under different light intensities. A temperature–humidity chamber (−70 to 150 °C, JHY-H-100L, China) provided extreme temperature conditions for performance testing. A universal testing machine (INSTRON 68SC-1, USA) assessed the tensile and compressive strength of the composites. The complex permittivity and permeability were evaluated using a vector network analyzer (VNA, 3674D, CETC, China) to characterize the electromagnetic wave absorption performance.

Radar cross-section (RCS) simulations were carried out using CST Studio Suite with an asymptotic solver under monostatic radar conditions. The incident electromagnetic wave was modeled as a plane wave, and the simulation frequency was set at 10 GHz for angular-dependent analysis. The material parameters used in the simulation were extracted from experimentally measured complex permittivity and permeability.

Experimental RCS measurements were conducted in a microwave anechoic chamber using scaled aircraft models coated with the MASA composite. The measurements were performed over the 5–12 GHz frequency range under both vertical and horizontal polarization modes. A vector network analyzer was used to collect the scattered signals, and standard calibration procedures were applied to obtain the RCS values.

2.5 Mechanical property characterization

A comprehensive understanding of the mechanical properties of coatings designed for integrated anti/de-icing and radar stealth applications is essential for their adoption in real-world implementation. These properties determine the composite's durability under operational stresses, as well as its compatibility with various substrates and geometries. Beyond tensile and compressive strength, the adhesion of the coating to various substrates plays a critical role in ensuring its service-life reliability [23].

In this work, both the standard mechanical properties and substrate-dependent adhesion strength of the composite film were systematically evaluated. Standardized tensile and compressive specimens were prepared via a mold casting and tested using a universal testing machine (Fig. S21(a) in the ESM). The composite film achieved an average tensile strength of 0.80 ± 0.5 MPa and a compressive strength of 7.08 ± 0.5 MPa, demonstrating superior performance under tensile and compressive loads (Fig. S20(c) in the ESM). To assess adhesion strength, the composite material was cast onto five common substrates, including aluminum, steel, copper, PTFE, and glass (Fig. S21(b) in the ESM). Comparative adhesion tests reveal that the composite film significantly outperforms pure PDMS, exhibiting markedly higher adhesion strength across all substrates (Fig. S21(d) in the ESM). This improvement is attributed to the inclusion of Fe_3O_4 and rGO, which enhance the interfacial bonding strength and increase the viscosity of the PDMS matrix.

The flexibility of the coating was further evaluated through bending, twisting, and rolling tests of 3 mm-thick samples (Figs. S21(e)–S21(g) in the ESM). These tests confirm the coating's exceptional adaptability to complex surfaces. The rGO@Fe_3O_4 hybrid network embedded in the PDMS matrix remains structurally stable under such mechanical deformation due to the elastomeric nature of the matrix, which helps preserve the conductive and magnetic pathways. As a result, the key functional properties, including microwave absorption and anti-icing performance, are expected to be maintained without significant degradation.

These evaluations confirm that the composite film achieves the dual functional requirements of anti-fouling and radar stealth while maintaining robust mechanical performance. Its strong adhesion with substrates, mechanical resilience, and flexibility enable reliable operation under extreme conditions, reinforcing its potential for real-world applications.

3 Results and discussion

3.1 Fabrication and anti-solid adhesion of MASA composite

We synthesized iron oxide (Fe_3O_4) nanoparticles via a solvothermal process and co-dispersed them with rGO nanosheets into the PDMS matrix. In particular, a hydroxylated surface modification strategy was implemented to tailor the conductivity, interfacial bonding strength, and colloidal dispersion stability of Fe_3O_4 nanoparticles. This chemical functionalization promotes strong electronic coupling interactions between the Fe_3O_4 nanoparticles and rGO nanosheets, resulting in the formation of a rich heterogeneous microstructure, akin to micro-capacitors, and the establishment of a uniform conductive network. This hybrid structure imparts both photothermal conversion and microwave absorption capabilities to the MASA composite. In addition, we conducted high-temperature swelling treatments (60 to 80 °C) to force the polymer network to absorb liquid paraffin. Upon returning to ambient or sub-ambient conditions, the swollen MASA composite automatically releases liquid paraffin to the surface via osmotic pressure, thereby enabling its solid-repellent property. Different MASA compositions can be tuned for materials performance optimization (Table S1 in the ESM). It is worth noting that liquid paraffin exhibits negligible dielectric and magnetic losses, as confirmed by both literature and our experimental measurements (Fig. S11 in the ESM). This indicates that paraffin is essentially transparent to electromagnetic waves and does not significantly interfere with impedance matching or microwave absorption performance. The fabrication process is illustrated in Fig. S5 in the ESM and Experimental. In addition to its anti-fouling capabilities, the MASA composite is further equipped with highly efficient photothermal ability by incorporating Fe_3O_4 nanoparticles and rGO as photothermal agents. These additives can achieve rapid surface heating, which facilitates efficient melting of various icing layers.

To evaluate the solid repellent performance of the MASA, particularly under cryogenic conditions, a multi-modal characterization protocol was implemented, focusing on several key aspects: the formation and regeneration of the lubricating film, anti-fouling performance, solar light absorption efficiency, ice adhesion strength, and durability. First, we can systematically tune the paraffin content percentage by controlling the swelling time (Fig. S6 in the ESM). The regenerative capability of the liquid paraffin film was characterized by using an optical microscope (see Figs. 2(a)–2(c) and Figs. S5–S7 in the ESM). The liquid paraffin migrates to the PDMS surface through the tiny channels in the polymer network by osmotic pressure, forming a lubricating film. When the interfacial lubricating film is removed, the liquid paraffin continuously diffuses out and rebalances the pressure [24]. After only 5 min of this self-repairing process, a dense lubricating film re-forms on the surface. Furthermore, we applied ice adhesion strength on MASA composites with different paraffin contents at −40 °C to determine the optimal paraffin content percentage, as shown in Fig. S8 in the ESM (gray bars) [25, 26]. Ice adhesion strength on MASA composite decreases with the increase of paraffin content, while it plateaus at ~ 10 kPa after the paraffin reaches 10 wt.%. As a result, 10 wt.% was identified as the optimal loading for subsequent tests.

The liquid paraffin in the MASA is confined within the polymer matrix and porous structure, which helps suppress rapid loss and enables a sustained self-replenishing surface layer. Although gradual depletion may occur under prolonged exposure to harsh environmental conditions (e.g., rain, elevated temperature, or mechanical wear), the loss rate is expected to be slow due to the confined nature of the liquid phase. Moreover, the system can be readily restored through re-infusion of the liquid paraffin, providing a feasible strategy for maintaining long-term performance in practical applications.

To assess anti-fouling performance, we quantified both the shear adhesion strength ($\tau = F/A$) and the normal adhesion strength ($\sigma = F/A$) of common solid foulants—including guano, mud, and insect residues—on both MASA and PDMS surfaces. The shear adhesion strength (Figs. 2(d)–2(f)), which reflects the tangential resistance during sliding removal, was consistently low on the MASA (~ 0.3 kPa) regardless of foulant type. In contrast, PDMS exhibited

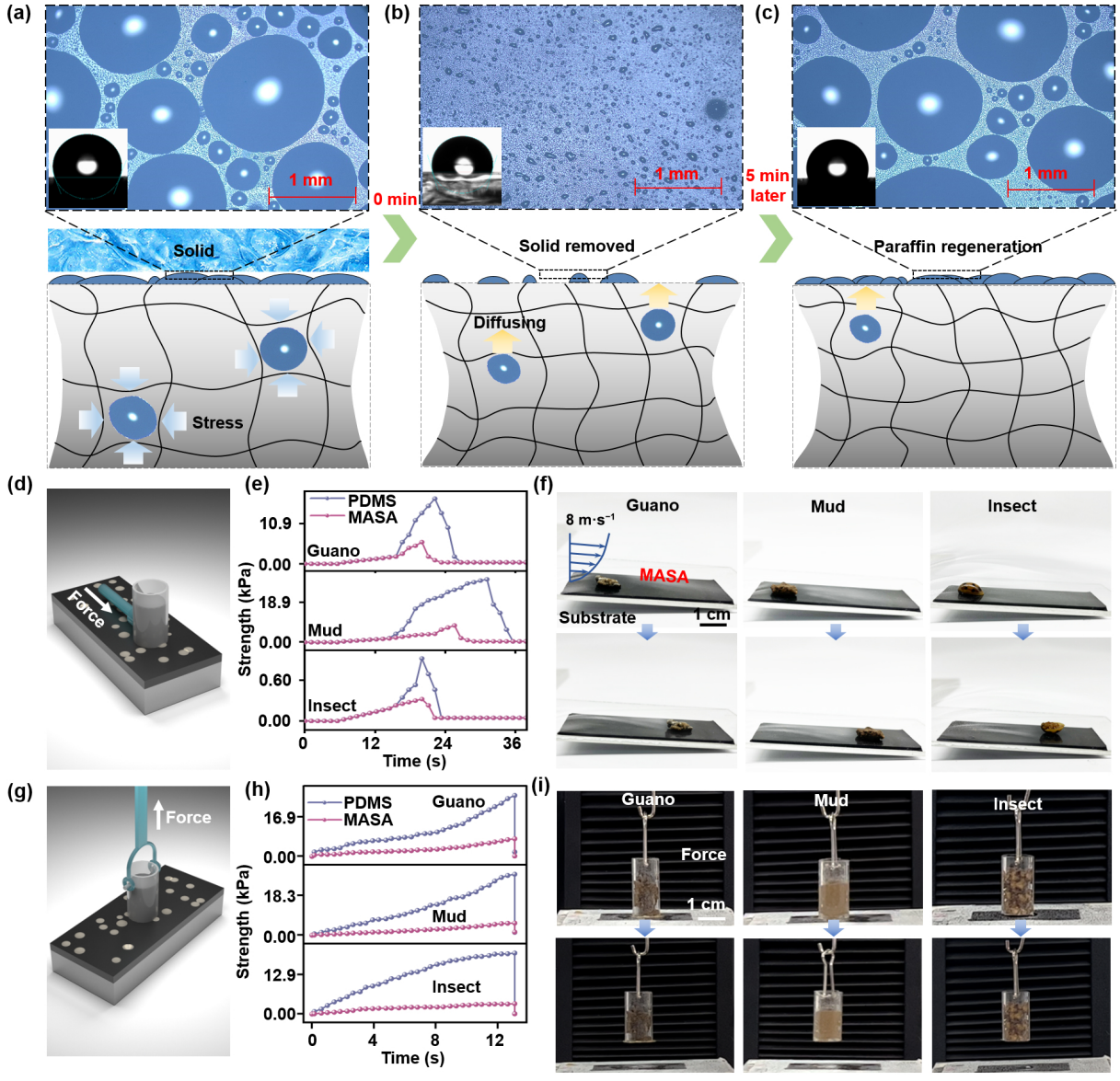

Figure 2 Solid repellent mechanism and performance of the MASA composite. (a) Pre-cleaning state: optical micrograph (top) and schematic (bottom) showing paraffin distribution on the surface and droplets trapped in the polymer network by the surface tension-induced pressure from the surface droplets. (b) Immediately post-sweeping: Inner droplets migrate toward the surface due to the pressure released. (c) Equilibrium state (5 min after sweeping): Redistributed paraffin achieves homogeneous surface coverage with continuous lubricant replenishment. (d)–(f) Shear adhesion strength (τ) of various solid contaminants. (g)–(i) Normal adhesion strength (σ) of various solid contaminants.

significantly higher shear strengths: 18 kPa for guano, 32 kPa for mud, and 0.8 kPa for insect residues. These results correspond to a > 60% reduction in shear strength on the MASA, highlighting its superior foulant-release capability. In addition, wind-blow experiments (Fig. 2(f)) at 8 m/s (Beaufort Scale: Force 5) demonstrated near-complete removal of foulants from the MASA surface, whereas PDMS retained substantial residues.

The normal adhesion strength (Figs. 2(g)–2(i)), representing the perpendicular detachment force, was also significantly reduced on the MASA (~ 2 kPa for all foulants) compared to ~ 24 kPa on PDMS, corresponding to an approximate 70% reduction. Furthermore, the MASA exhibits excellent liquid repellency toward liquids with different surface tensions (Fig. S9 in the ESM). For instance, water and silicone oil droplets slide on the MASA within 5 s (12 mm/s) and 45 s (1.33 mm/s), respectively, at a sliding angle of 12°, whereas on PDMS, the corresponding sliding times are 14 s (4.29 mm/s) and 76 s (0.76 mm/s). These results demonstrate that the paraffin-induced slippery interface significantly enhances the self-cleaning capability of the MASA.

3.2 Photothermal de-icing of MASA composite

To systematically evaluate the photothermal conversion efficiency, we fabricated PDMS-based composites with controlled rGO@Fe_3O_4 (0.5 wt.% to 15 wt.%) and subjected them to standardized solar irradiation (100 mW/cm^2), as shown in Fig. 3(a). Low-temperature test results (−30 ± 1 °C) revealed that the MASA with even 0.5 wt.% can achieve 94% of the maximum photothermal efficiency. The MASA with higher rGO@Fe_3O_4 content (0.5 wt.%–15 wt.%) can initiate phase-change rapidly, reaching 0 °C within 120 s. Subsequently, it achieved a steady state of 16 ± 0.5 °C after

500 s of irradiation (Fig. 3(b)). In addition, our facile fabrication method can easily manufacture large-area (100 cm × 30 cm) MASA films. Such large-scale MASA films can demonstrate stable and uniform heating performance under natural sunlight (63 mW/cm^2), quantified by infrared thermography (Fig. 3(c)). Furthermore, the effect of varying liquid paraffin content on MASA's photothermal performance was also examined. As shown in Fig. S10 in the ESM, the incorporation of liquid paraffin does not compromise the photothermal efficiency. To inform practical applications, the phase transition behavior of MASA under varying light intensities and environmental temperatures was also explored. The phase diagram of MASA (Fig. 3(d)) delineates 3 surface temperature zones: freezing, ice-water mixture, and melting. By integrating this phase diagram with specific environmental conditions, we can predict surface temperature precisely and determine the necessity for supplementary anti/de-icing measures. In particular, we have explored icing-delay time on the MASA, a key parameter of photothermal anti/de-icing, representing the duration required for water to freeze on the cooled substrate. This delay of icing provides a critical "window" for de-icing operations. Therefore, a longer delay time enables easier ice removal before detrimental accumulation of ice occurs. In this case, MASA provides a sufficient de-icing window (≥ 1000 s) under various low-temperature conditions when solar irradiance is one sun (100 mW/cm^2) (Fig. 3(e)). At an ultralow temperature of −60 °C with a relatively low solar flux of 0.2 sun (20 mW/cm^2), freezing occurred within 10 s. If the solar flux increases to 1.0 sun, the freeze-delay time can still reach ~ 1000 s.

Reducing ice adhesion strength is another critical method for efficient de-icing. With solar irradiation, ice adhesion strength can be further reduced from ~ 10 to ~3 kPa, regardless of paraffin concentration (Fig. S8 in the ESM). We also explored the temperature dependency of MASA in the ice adhesion (Fig. 3(f)). Without solar irradiation, ice adhesion strength exhibits a marginal increase as environmental temperature decreases, but remains < 10 kPa, highlighting MASA's low ice adhesion across a wide

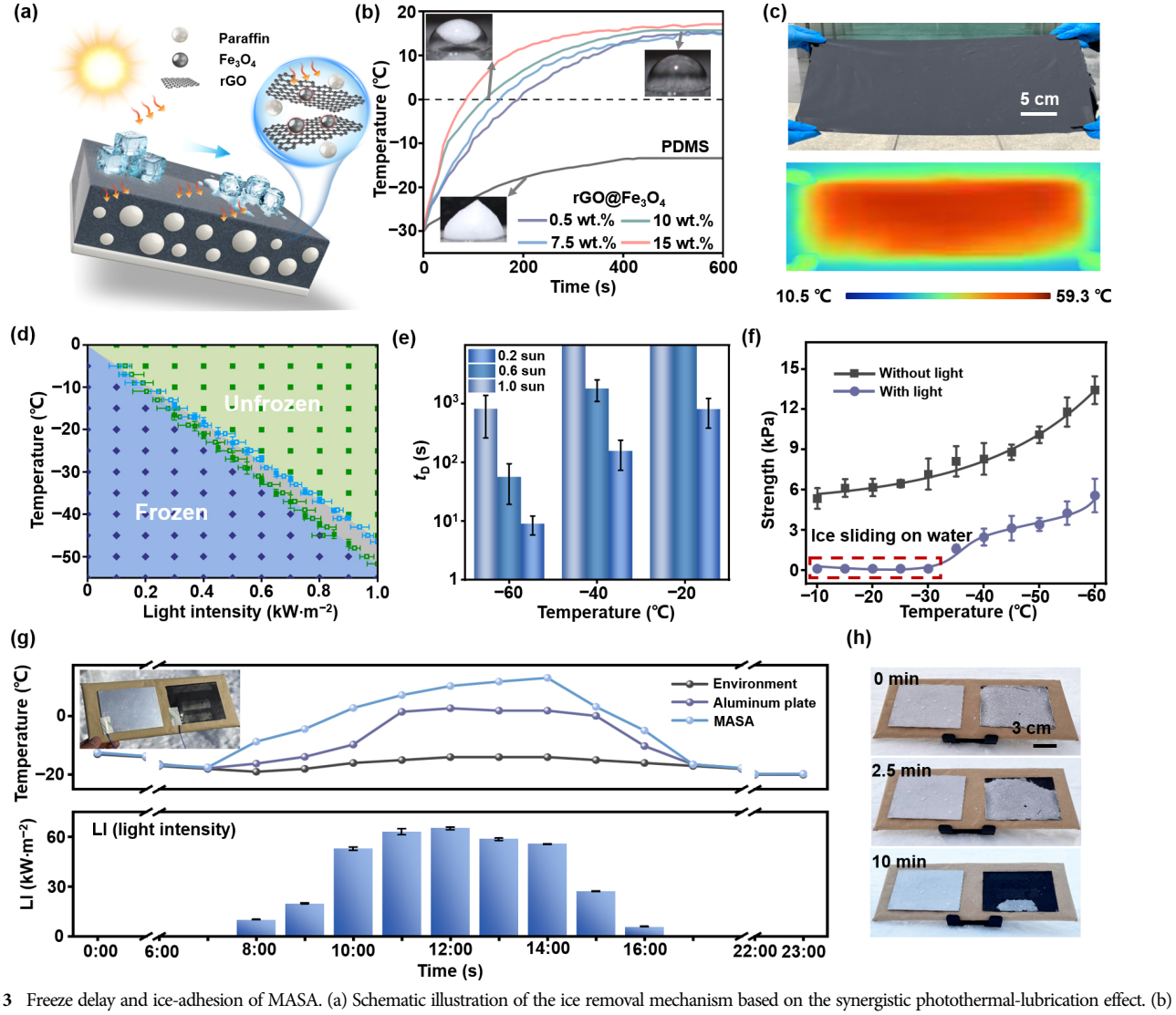

Figure 3 Freeze delay and ice-adhesion of MASA. (a) Schematic illustration of the ice removal mechanism based on the synergistic photothermal-lubrication effect. (b) Evaluation of surface temperature rise among three different coatings under simulated sunlight. (c) Demonstration of a large-area MASA film, shown by a physical image (top) and infrared thermal image (bottom) under standard solar illumination (1 sun). (d) Phase diagram of MASA in its frozen state across various light intensities and temperature conditions. (e) Time delay for ice formation under varying solar irradiance levels. (f) Comparison of ice adhesion strength under conditions with and without light exposure, and ((g) and (h)) experimental demonstrations of the defrosting and de-icing performance of MASA. The error bars were obtained from at least 3 independent measurements.

temperature range. Under solar irradiation, ice adhesion strength is further reduced owing to the solar heating, which weakens the interface bond. In particular, when the environmental temperature exceeds −35 °C, the surface temperature of MASA rose above 0 °C, forming a liquid layer at the ice-coating interface, which significantly enhances ice sliding and thereby improves de-icing efficiency.

Practical implementations of anti/de-icing mostly require mechanical durability and service life [25]. We applied 20 freezing-de-icing cycles at −35 °C on the MASA (Fig. S10(b) in the ESM), and found no significant increase in ice adhesion strength, demonstrating its long-term reliability. MASA was also applied to aluminum plates for de-icing tests at −18 °C (Figs. 3(g) and 3(h)). The outdoor experiments were conducted in Beijing, China, on a clear winter day, January 11, to simulate realistic cold-climate conditions under natural solar irradiation. To evaluate its real-world performance under natural solar irradiation, we monitored the solar illumination intensity and simultaneously recorded the surface temperatures of both the MASA and bare aluminum plates during a full daytime cycle. The data showed that, owing to its photothermal conversion capability, the surface temperature of MASA remained above 0 °C between 10:00 and 15:00, even under ambient subzero conditions. This temperature range corresponds to the effective de-icing window, during which solar-driven heating enables passive de-icing without the need for external power input, thus offering a sustainable and energy-efficient anti-/de-icing strategy. As shown in Fig. 3(h), an outdoor de-icing comparison experiment was carried out at 14:00, when the solar irradiance was approximately 55.8 ± 0.2 mW·cm^{-2} and the ambient temperature was 14 °C. Under these conditions, the MASA surface, initially fully covered with ice, began to melt within 2.5 min of solar exposure. After 10 min of illumination, the ice was almost completely removed, further confirming MASA's superior photothermal-assisted de-icing performance. This passive de-icing strategy minimizes energy consumption and is promising for sustainable applications in cold environments.

3.3 Radar stealth performance

The Fe_3O_4 nanoparticles can strongly enhance interfacial polarization, electron transitions, and conductive losses, thereby significantly improving the material's microwave absorption properties (Fig. 4(a)) [26–30]. Based on the magnetic loss theory, the electromagnetic absorbance mechanisms in MASA were mainly attributed to natural resonance, exchange resonance, and eddy current effect. In particular, the eddy current loss parameter C_0 was calculated via Eq. (1) [31]

$$C_0 = \mu''(\mu')^{-2} f^{-1} \quad (1)$$

where μ'' denotes the imaginary part of permeability, μ' is the real part of the permeability of the material, and f is the electromagnetic wave frequency. A constant C_0 should be expected if eddy current losses are the predominant source of magnetic dissipation in the MASA composite, as shown in Fig. 4(b). The experimentally observed C_0 exhibited frequency-dependent oscillations, demonstrating that the magnetic dissipation of the material was not only due to eddy current losses but also natural resonance and exchange resonance [32].

In addition, the attenuation constant α can be expressed as

$$\alpha = \frac{\sqrt{2}\pi f}{c}\sqrt{(\mu''\varepsilon'' - \mu'\varepsilon') + \sqrt{(\mu''\varepsilon'' - \mu'\varepsilon')^2 + (\mu'\varepsilon'' + \mu''\varepsilon')^2}} \quad (2)$$

where c represents the speed of light in a vacuum, ε'' is the imaginary part of permittivity, and ε' is the real part, the attenuation constant α quantifies the rate of electromagnetic energy dissipation as waves propagate through a material. A higher α indicates more efficient wave absorption, which is particularly significant for stealth technology and electromagnetic shielding. By analyzing the frequency dependence of α (Fig. 4(b)), we assessed the MASA composite's attenuation performance. As frequency increases, α exhibits a clear upward trend, suggesting enhanced dissipation in the high-frequency range. This improvement originates from intensified dielectric losses—stemming from interfacial polarization and conductive loss within the rGO@Fe_3O_4 network that raise ε''—as well as magnetic losses via natural and exchange resonance. These synergistic effects collectively strengthen the composite's attenuation capability at higher frequencies.

The Cole–Cole plot (Fig. 4(c)) provides further insight into the dielectric relaxation behavior of MASA, exhibiting a typical semicircular arc with a linear tail. This pattern indicates that the dielectric loss originates primarily from three mechanisms: (1) interfacial polarization at the boundary between Fe_3O_4 nanoparticles and rGO sheets, arising from the accumulation of space charges in heterogeneous domains; (2) dipolar polarization caused by structural defects and functional groups within rGO, which can align with alternating fields at specific frequencies; and (3) conduction loss, facilitated by the formation of a continuous conductive network formed by rGO and Fe_3O_4 in the PDMS matrix, which promotes electron hopping and leakage current [23]. These synergistic mechanisms contribute to broadband dielectric dissipation across the frequency spectrum.

The microwave absorption capabilities of materials are typically assessed using a vector network analyzer to measure the material's electromagnetic parameters, including complex permittivity (ε) and permeability (μ). MASA with different compositions develops varying corresponding electromagnetic parameters, as shown in Fig. 4(d) and Fig. S12 in the ESM. In particular, with the increase of the rGO content, both the real and imaginary components of the complex permittivity exhibited an upward trend, primarily resulting from the enhanced conductivity induced by the rGO. Similarly, the permeability of the MASA varies with increasing Fe_3O_4 content, mainly owing to the intrinsic ferromagnetism of Fe_3O_4, which facilitates magnetic loss mechanisms such as domain wall motion, natural ferromagnetic resonance, and spin rotation. In contrast, the variation in permittivity is primarily attributed to interfacial polarization and conductive loss (electron hopping) arising from the incorporation of Fe_3O_4 and its interaction with the rGO network. The combined dielectric and magnetic responses jointly determine the electromagnetic attenuation capability and impedance matching, thereby governing the overall microwave absorption performance of the material. To quantitatively evaluate the microwave absorption performance of the MASA across the 2–18 GHz frequency range, the reflection loss (RL) is calculated using transmission line theory and expressed as [23]

$$Z_1 = Z_0\sqrt{(\mu_r/\varepsilon_r)}\tanh\left[j(2\pi fd/c)\sqrt{\mu_r\varepsilon_r}\right] \quad (3)$$

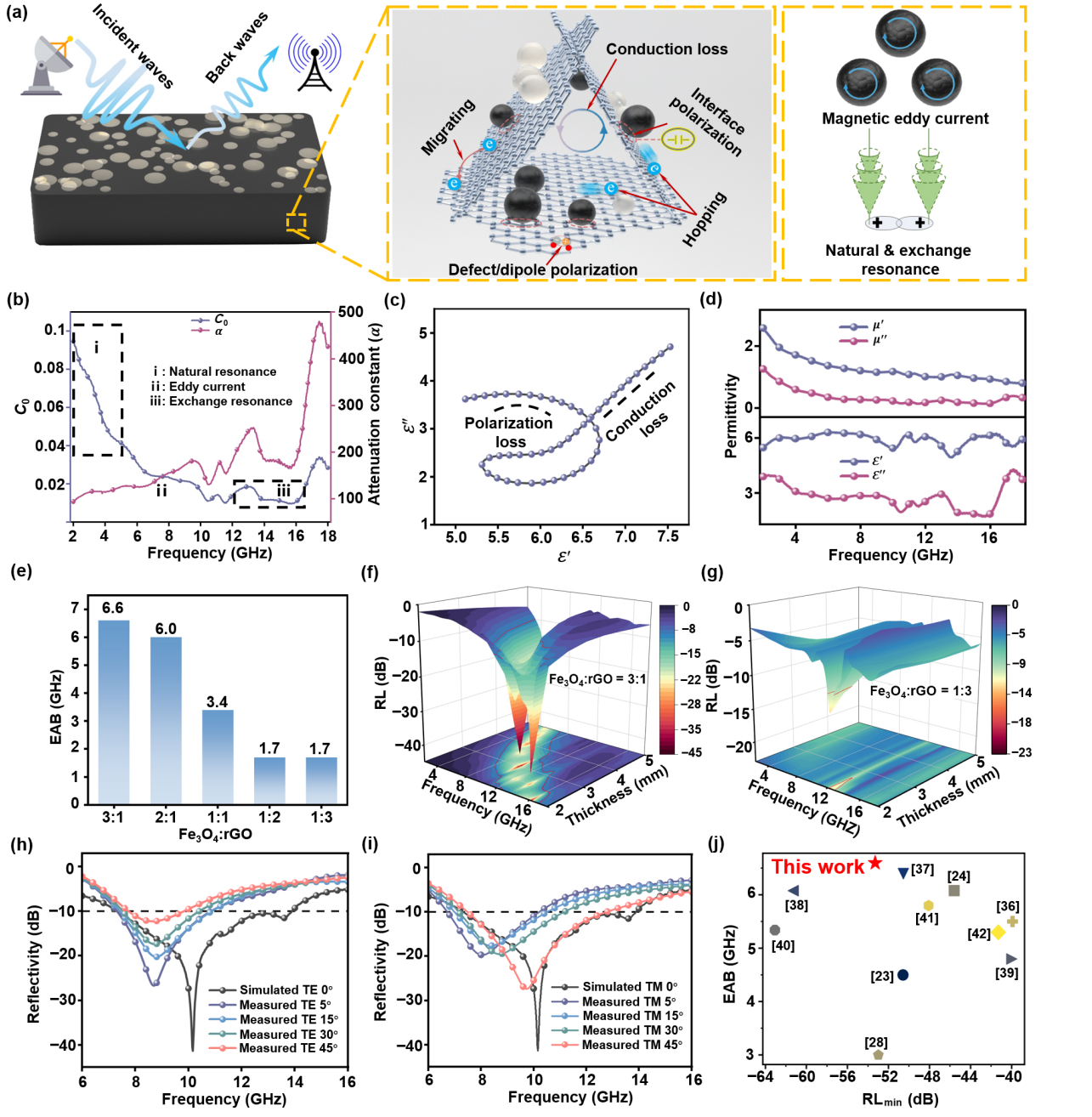

Figure 4 Multiscale analysis of microwave absorption mechanism in MASA. (a) Electromagnetic wave loss mechanism illustrating energy dissipation pathways, (b) Frequency dispersion curves of eddy current loss parameter (C_0) and attenuation constant (α), (c) Cole–Cole diagram of MASA, (d) Electromagnetic parameters, including relative permittivity and permeability of MASA across a measured frequency range. (e) Comparison of the effective absorption bandwidth of various MASA. (f) and (g) Reflection loss characteristics of MASA at varying thicknesses with special ratios. (h) and (i) Reflectivity measurements of MASA under TE and TM polarization modes. (j) Overall performance of MASA against other reported microwave absorbing materials.

$$\mathrm{RL} = -20\lg\left|\frac{Z_1 - Z_0}{Z_1 + Z_0}\right| \tag{4}$$

where Z_1 and Z_0 represent the input impedance of the absorber and the free space impedance, d is the absorber thickness, while $\varepsilon_r = \varepsilon' + j\varepsilon''$ and $\mu_r = \mu' + j\mu''$ correspond to the relative permittivity and relative permeability derived from the experiment measurements. The calculated reflection losses for the MASA with Fe_3O_4-to-rGO ratio are shown in Figs. 4(e)–4(g) and Fig. S13 in the ESM. These results indicate that microwave absorption in the MASA composite is governed by a balance between conductive loss and impedance matching, rather than by simply maximizing filler content. Increasing rGO content enhances dielectric loss by improving electrical conductivity; however, excessive conductivity leads to severe impedance mismatch, preventing incident electromagnetic waves from entering the absorber effectively. Consequently, both the effective absorption bandwidth and peak reflection loss are degraded at high rGO loadings.

This behavior confirms the existence of an optimal rGO–Fe_3O_4 synergistic regime. Here, the "synergistic effect" does not refer to a simple linear superposition of dielectric and magnetic losses, but rather to the cooperative optimization of impedance matching,

attenuation capability, and interfacial polarization. Specifically, excessive rGO content results in over-conductive networks and poor impedance matching, whereas Fe_3O_4-rich systems may suffer from insufficient dielectric loss. The optimized rGO@Fe_3O_4 hybrid therefore enables balanced coupling between dielectric loss, magnetic response, and interfacial polarization, leading to enhanced microwave absorption performance. Similar mechanisms have been widely reported in hybrid dielectric–magnetic absorbers [33–35].

Accordingly, the MASA sample with the lowest rGO content exhibits the best absorption performance, achieving an EAB of 6.6 GHz at a thickness of 3 mm, which fully covers the X-band, and a minimum RL of −41.3 dB, corresponding to more than 99.99% absorption under the metal-backed condition. In contrast, samples with higher rGO contents show degraded impedance matching and weaker absorption characteristics. Based on the comprehensive consideration of absorber thickness, EAB, and minimum RL, the composition containing PDMS/paraffin, 2.5 wt.% rGO, and 7.5 wt.% Fe_3O_4 at a thickness of 3 mm was selected for further investigation.

Taken together, the optimized rGO@Fe_3O_4 hybrid network provides a loss-balanced absorption pathway, in which interfacial polarization and magnetic response contribute to electromagnetic attenuation while appropriate conductivity preserves favorable impedance matching. The thickness-dependent RL behavior can be further understood using the quarter-wavelength matching model: as the absorber thickness increases, the absorption peak shifts toward lower frequencies and the EAB becomes narrower. This trend indicates that both material composition and structural thickness play important roles in determining the impedance matching condition and attenuation path of incident electromagnetic waves. Therefore, the superior absorption performance of the low-rGO MASA sample originates from balanced dielectric–magnetic loss and impedance matching, rather than from excessive dielectric dissipation.

To evaluate the mechanical stability of the conductive/magnetic network, cyclic compression tests were conducted on the representative MASA sample containing 2.5 wt.% rGO and 7.5 wt.% Fe_3O_4. After 400 loading–unloading cycles, the electromagnetic parameters showed negligible variation, confirming the robustness of the internal conductive/magnetic network under repeated mechanical deformation (Fig. S16 in the ESM).

A MASA sample with a thickness of 3 mm was then prepared, and its reflectance was measured using the bowtie antenna method (Fig. S17 in the ESM). The corresponding results are presented in Figs. 4(h) and 4(i). The data show that under transverse electric (TE) polarization, the EAB decreases with increasing incident angle, whereas under transverse magnetic (TM) polarization, the EAB broadens. These results demonstrate excellent angular and polarization stability of the MASA composite.

Moreover, compared to most reported materials, the MASA composite exhibits a broader effective absorption bandwidth and a deeper minimum reflection loss, highlighting its outstanding capability for broadband and high-efficiency electromagnetic wave absorption (Fig. 4(j)). Notably, this performance is achieved at a relatively small thickness, demonstrating a favorable balance between thickness and EAB compared with previously reported materials [24, 25, 29, 36–42].

Given PDMS's superior flexibility and environmental stability, it serves as an ideal substrate for microwave absorbers. These properties not only ensure excellent robustness but also enable conformal coating on complex geometries, including both flat and curved surfaces. To evaluate MASA's RCS, we applied MASA to three distinct model surfaces: a flat plate model, the NASA standard model, and a fighter jet model (Fig. 5(a) and Figs. S18–S20 in the ESM). As shown in Figs. 5(a) and 5(b), after the aircraft skin is coated with the MASA, the induced surface-current amplitude on the metallic surface becomes lower. This occurs because the MASA effectively dissipates the incident electromagnetic energy inside the coating through dielectric and magnetic losses, thereby reducing the electromagnetic energy that reaches the metal and consequently weakening its secondary reflection. By comparing the changes in RCS under both horizontal and vertical polarization in the X-band, the MASA achieved substantial RCS reduction across different morphologies [34]. The angular-dependent RCS results shown in Figs. 5(c) and 5(d) were obtained at a fixed frequency of 10 GHz, where the average RCS reductions reached 13.47/13.17 dB in the two polarization modes (flat plate), 18.95/17.36 dB (NASA Almond), and 19.17/20.0 dB (fighter jet), demonstrating shape-adaptive stealth performance. In addition, broadband RCS measurements were conducted over the frequency range of 5–12 GHz, as shown in Figs. 5(f) and 5(g). Validation on an 18:1 scaled F-117 model showed RCS reductions of 8.15 dB (horizontal) and 5.50 dB (vertical), confirming the effectiveness of MASA in practical broadband stealth applications.Given PDMS's superior flexibility and environmental stability, it serves as an ideal substrate for microwave absorbers. These properties not only ensure excellent robustness but also enable conformal coating on complex geometries, including both flat and curved surfaces. To evaluate MASA's RCS, we applied MASA to three distinct model surfaces: a flat plate model, the NASA standard model, and a fighter jet model (Fig. 5(a) and Figs. S18–S20 in the ESM). As shown in Figs. 5(a) and 5(b), after the aircraft skin is coated with the MASA, the induced surface-current amplitude on the metallic surface becomes lower. This occurs because the MASA effectively dissipates the incident electromagnetic energy inside the coating through dielectric and magnetic losses, thereby reducing the electromagnetic energy that reaches the metal and consequently weakening its secondary reflection. By comparing the changes in RCS under both horizontal and vertical polarization in the X-band, the MASA achieved substantial RCS reduction across different morphologies [34]. The angular-dependent RCS results shown in Figs. 5(c) and 5(d) were obtained at a fixed frequency of 10 GHz, where the average RCS reductions reached 13.47/13.17 dB in the two polarization modes (flat plate), 18.95/17.36 dB (NASA Almond), and 19.17/20.0 dB (fighter jet), demonstrating shape-adaptive stealth performance. In addition, broadband RCS measurements were conducted over the frequency range of 5–12 GHz, as shown in Figs. 5(f) and 5(g). Validation on an 18:1 scaled F-117 model showed RCS reductions of 8.15 dB (horizontal) and 5.50 dB (vertical), confirming the effectiveness of MASA in practical broadband stealth applications.

Beyond electromagnetic stealth, MASA demonstrates outstanding solar-driven de-icing capability even at −20 °C. Under 1 sun illumination (Figs. 5(h) and 5(i)), frost on a flat MASA-coated substrate completely disappears within 102 s, while a scaled fighter-jet model achieves an ice-free surface in only 200 s. This rapid thawing at sub-zero temperatures stems from MASA's potent photothermal conversion and highly efficient interfacial heat transfer, highlighting its dual-role potential for aerospace and

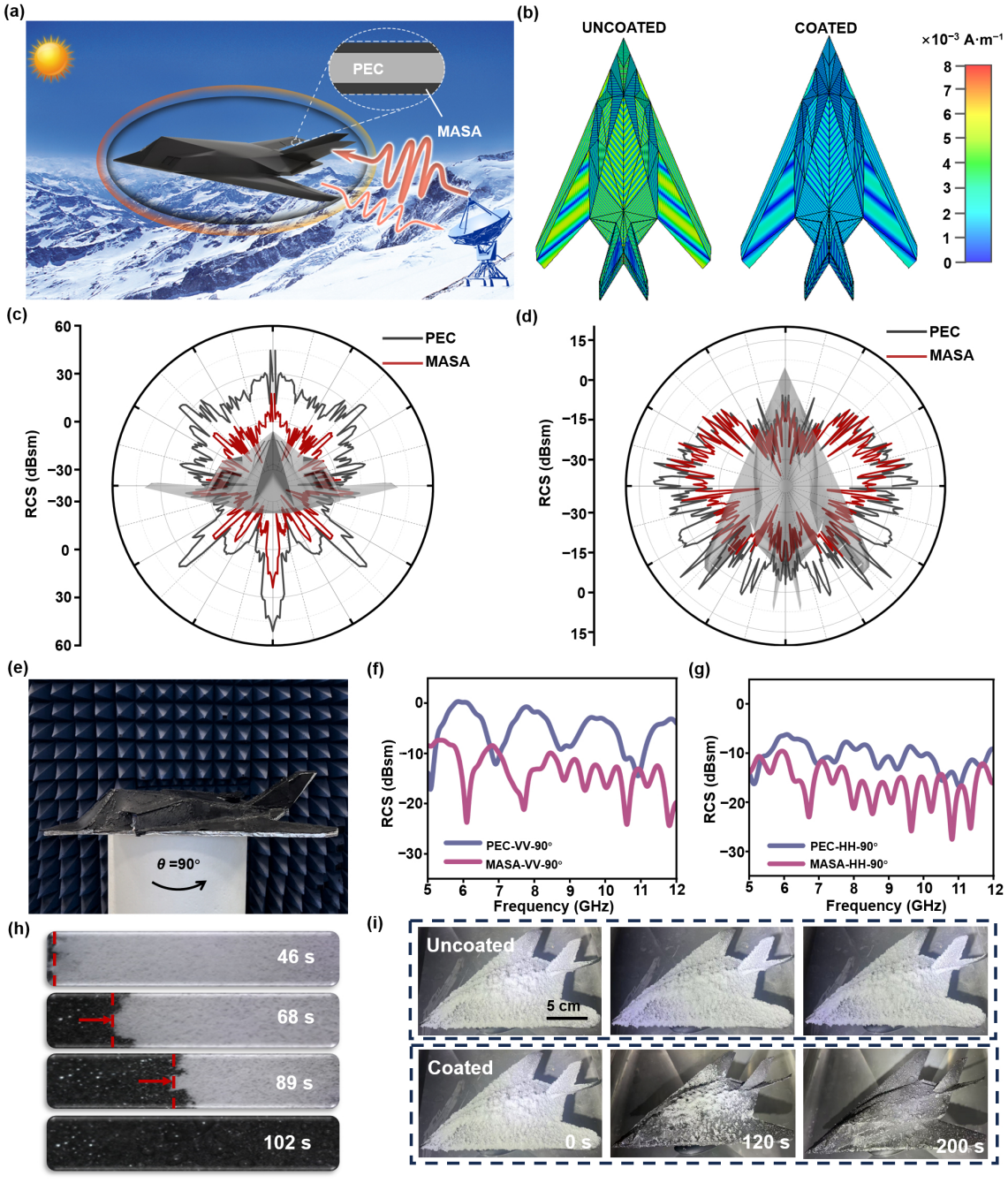

Figure 5 Radar stealth performance analysis of MASA. (a) Schematic of a MASA coted fighter aircraft model, demonstrating the application concept, (b) simulated surface current distribution on uncoated vs. MASA-coated fighter aircraft, (c) simulated RCS results at 10 GHz for various roll angles with perfect electric conductor (PEC) and MASA-coated aircraft, (d) simulated RCS results at a fixed frequency of 10 GHz for various azimuth angles with PEC and MASA-coated aircraft, (e) photograph of MASA coated aircraft, (f) and (g) broadband RCS measurement results in the frequency range of 5–12 GHz under vertical and horizontal polarization at an azimuth angle of 90°, and (h) and (i) experimental demonstrations of the defrosting and de-icing performance of MASA.

military platforms operating in extreme cold and high-radiation environments.

4 Conclusions

This study presents a rationally designed, multifunctional composite material achieved by integrating hydroxylated Fe_3O_4 nanoparticles with reduced rGO. Through controlled solvothermal hydroxylation, the dispersion of nanoparticles and interfacial bonding are significantly enhanced, leading to notable improvements in both electromagnetic and mechanical performance. By incorporating a bioinspired paraffin-based lubricating surface and leveraging photothermal effects, the composite exhibits outstanding anti-/de-icing capabilities, maintaining self-regenerating lubrication and reduced ice adhesion over more than 20 freeze-thaw cycles under extreme environmental conditions.

Under optimal formulation (10 wt.% filler, 3 mm thickness), the material demonstrates a wide EAB of 6.6 GHz and a maximum reflection loss of −41.3 dB, confirming its excellent microwave

absorption capacity. RCS measurements further reveal strong stealth functionality, with average reductions of 8.35 dB (horizontal polarization) and 5.5 dB (vertical polarization) in the 5–12 GHz frequency range. Moreover, the composite exhibits robust adhesion across a variety of substrates, underscoring its adaptability as a high-performance coating.

Overall, this work introduces a novel, robust, and multifunctional material that effectively integrates electromagnetic stealth, environmental resilience, and mechanical durability. These findings lay a solid foundation for the development of advanced materials tailored for harsh environments, with promising applications in military, aerospace, and next-generation engineering systems.

Electronic Supplementary Material: Supplementary material (synthesis route and composition details of MASA composites; structural, morphological, and chemical characterizations of Fe_3O_4 and rGO@Fe_3O_4; paraffin distribution and self-regeneration behavior; wettability, anti-fouling, ice adhesion, and freeze–de-icing performance; photothermal properties under different irradiation and temperature conditions; electromagnetic parameters, reflection loss, effective absorption bandwidth, and matching thickness analysis; RCS simulation and measurement details; mechanical properties, substrate adhesion, flexibility, and cyclic compression stability) is available in the online version of this article at https://doi.org/10.26599/NR.2026.94908933.

Data availability

All data needed to support the conclusions in the paper are presented in the manuscript and the Electronic Supplementary Material. Additional data related to this paper may be requested from the corresponding author upon request.

Acknowledgements

This work is supported by the National Natural Science Foundation of China (No. 12002006).

Declaration of competing interest

All the contributing authors report no conflict of interests in this work.

Author contribution statement

H. Y. D.: Data curation, validation, writing manuscript, experimental design. T. T. H.: Data curation, validation, writing manuscript, experimental design. Y. X. C.: Manuscript discussions, revised manuscript. Y. X. H.: Conception, funding acquisition, writing manuscript. J. W.: Conception, funding acquisition, writing manuscript. Z. Y. H.: Conception, funding acquisition, writing manuscript. All the authors have approved the final manuscript.

Use of AI statement

None.

References

[1] Kreder, M. J.; Alvarenga, J.; Kim, P.; Aizenberg, J. Design of anti-icing surfaces: Smooth, textured or slippery. *Nat. Rev. Mat.* **2016**, *1*, 15003.

[2] Dhyani, A.; Wang, J.; Halvey, A. K.; Macdonald, B.; Mehta, G.; Tuteja, A. Design and applications of surfaces that control the accretion of matter. *Science* **2021**, *373*, eaba5010.

[3] He, Z. W.; Xie, H. M.; Jamil, M. I.; Li, T.; Zhang, Q. H. Electro-/photo-thermal promoted anti-icing materials: A new strategy combined with passive anti-icing and active de-icing. *Adv. Mat. Interfaces* **2022**, *9*, 2200275.

[4] Wang, Y. L.; Yao, X.; Chen, J.; He, Z. Y.; Liu, J.; Li, Q. Y.; Wang, J. J.; Jiang, L. Organogel as durable anti-icing coatings. *Sci. China Mater.* **2015**, *58*, 559–565.

[5] Wu, C. Y.; Geng, H. Y.; Tan, S. C.; Lv, J. Y.; Wang, H. Q.; He, Z. Y., Wang, J. J. Highly efficient solar anti-icing/deicing via a hierarchical structured surface. *Mater. Horiz.* **2020**, *7*, 2097–2104.

[6] Zheng, W. W.; Teng, L.; Lai, Y. K.; Zhu, T. X.; Li, S. H.; Wu, X. W.; Cai, W. L.; Chen, Z.; Huang, J. Y. Magnetic responsive and flexible composite superhydrophobic photothermal film for passive anti-icing/active deicing. *Chem. Eng. J.* **2022**, *427*, 130922.

[7] Wang, L.; Gong, Q. H.; Zhan, S. H.; Jiang, L.; Zheng, Y. M. Robust anti-icing performance of a flexible superhydrophobic surface. *Adv. Mater.* **2016**, *28*, 7729–7735.

[8] Zhao, Z. H.; Chen, H. W.; Zhu, Y. T.; Liu, X. L.; Wang, Z. L. L.; Chen, J. C. A robust superhydrophobic anti-icing/de-icing composite coating with electrothermal and auxiliary photothermal performances. *Compos. Sci. Technol.* **2022**, *227*, 109578.

[9] Heydari, G.; Thormann, E.; Järn, M.; Tyrode, E.; Claesson, P. Hydrophobic surfaces: Topography effects on wetting by supercooled water and freezing delay. *J. Phys. Chem. C* **2013**, *117*, 21752–21762.

[10] Maitra, T.; Antonini, C.; Tiwari, M. K.; Mularczyk, A.; Imeri, Z.; Schoch, P.; Poulikakos, D. Supercooled water drops impacting superhydrophobic textures. *Langmuir* **2014**, *30*, 10855–10861.

[11] Lian, Z. X.; Cheng, Y.; Liu, Z. M.; Cai, Q. Q.; Tao, J.; Xu, J. K.; Tian, Y. L.; Yu, H. D. Scalable fabrication of superhydrophobic armor microstructure arrays with enhanced tribocorrosion performance via maskless electrochemical machining. *Surf. Coat. Technol.* **2023**, *461*, 129427.

[12] Jiang, J. W.; Shen, Y. Z.; Xu, Y. J. S.; Wang, Z.; Tao, J.; Liu, S. Y.; Liu, W. L.; Chen, H. F. An energy-free strategy to elevate anti-icing performance of superhydrophobic materials through interfacial airflow manipulation. *Nat. Commun.* **2024**, *15*, 777.

[13] Mitridis, E.; Schutzius, T. M.; Sicher, A.; Hail, C. U.; Eghlidi, H.; Poulikakos, D. Metasurfaces leveraging solar energy for icephobicity. *ACS Nano* **2018**, *12*, 7009–7017.

[14] Wu, S. W.; Liang, Z. Y.; Li, Y. P.; Chay, S.; He, Z. Y.; Tan, S. C., Wang, J. J.; Zhu, X. Y.; He, X. M. Transparent, photothermal, and icephobic surfaces via layer-by-layer assembly. *Adv. Sci.* **2022**, *9*, 2105986.

[15] Hou, M. T.; Jiang, Z. Y.; Sun, W.; Chen, Z. H.; Chu, F. Q.; Lai, N. C. Efficient photothermal anti-/deicing enabled by 3D $Cu_{2-x}S$ encapsulated phase change materials mixed superhydrophobic coatings. *Adv. Mater.* **2024**, *36*, 2310312.

[16] Urata, C.; Dunderdale, G. J.; England, M. W.; Hozumi, A. Self-lubricating organogels (SLUGs) with exceptional syneresis-induced anti-sticking properties against viscous emulsions and ices. *J. Mater. Chem. A* **2015**, *3*, 12626–12630.

[17] Zhang, Y. H.; Dong, H. Y.; Yu, C.; Wang, Z. C.; Huang, Y. X. Metastructure based broadband structural stealth with material–structure–function integration. *Compos. Sci. Technol.* **2024**, *253*, 110661.

[18] Zhang, T. Y.; Qiu, J. F.; Wang, S. H.; Juan, Y.; Li, J. Y.; Wang, W. Multi-scale engineering for enhancing broadband microwave absorption, electromagnetic shielding and infrared stealth of Ag NWs/N-doped rGO aerogels. *Adv. Funct. Mater.* **2026**, *36*, e21010.

[19] Liang, L. Y.; Li, Q. M.; Yan, X.; Feng, Y. Z.; Wang, Y. M.; Zhang, H. B.; Zhou, X. P.; Liu, C. T.; Shen, C. Y.; Xie, X. L. Multifunctional

magnetic $Ti_3C_2T_x$ MXene/graphene aerogel with superior electromagnetic wave absorption performance. *ACS Nano* **2021**, *15*, 6622–6632.

[20] Zhu, X. J.; Dong, Y. Y.; Xiang, Z.; Cai, L.; Pan, F.; Zhang, X.; Shi, Z.; Lu, W. Morphology-controllable synthesis of polyurethane-derived highly cross-linked 3D networks for multifunctional and efficient electromagnetic wave absorption. *Carbon* **2021**, *182*, 254–264.

[21] Cai, Z. X.; Su, L.; Wang, H. J.; Xie, Q.; Gao, H. F.; Niu, M.; Lu, D. Hierarchically assembled carbon microtube@SiC nanowire/Ni nanoparticle aerogel for highly efficient electromagnetic wave absorption and multifunction. *Carbon* **2022**, *191*, 227–235.

[22] Wang, X. H.; Yuan, Y.; Sun, X. X.; Qiang, R.; Xu, Y. C.; Ma, Y.; Zhang, E. S.; Li, Y. B. Lightweight, flexible, and thermal insulating carbon/SiO_2@CNTs composite aerogel for high-efficiency microwave absorption. *Small* **2024**, *20*, 2311657.

[23] You, W. B.; Pei, K.; Yang, L. T.; Li, X.; Shi, X. F.; Yu, X. F.; Guo, H. Q.; Che, R. C. *In situ* dynamics response mechanism of the tunable length-diameter ratio nanochains for excellent microwave absorber. *Nano Res.* **2020**, *13*, 72–78.

[24] Cui, J. X.; Daniel, D.; Grinthal, A.; Lin, K. X.; Aizenberg, J. Dynamic polymer systems with self-regulated secretion for the control of surface properties and material healing. *Nat. Mater.* **2015**, *14*, 790–795.

[25] Makkonen, L. Ice adhesion-theory, measurements and countermeasures. *J. Adhes. Sci. Technol.* **2012**, *26*, 413–445.

[26] Li, S.; Hou, Y. M.; Kappl, M.; Steffen, W.; Liu, J.; Butt, H. J. Vapor lubrication for reducing water and ice adhesion on poly(dimethylsiloxane) brushes. *Adv. Mater.* **2022**, *34*, 2203242.

[27] Green, M.; Liu, Z. Q.; Xiang, P.; Liu, Y.; Zhou, M. J.; Tan, X. Y.; Huang, F. Q.; Liu, L.; Chen, X. B. Doped, conductive SiO_2 nanoparticles for large microwave absorption. *Light: Sci. Appl.* **2018**, *7*, 87.

[28] Li, Y.; Liu, X. F.; Nie, X. Y.; Yang, W. W.; Wang, Y. D.; Yu, R. H.; Shui, J. L. Multifunctional organic–inorganic hybrid aerogel for self-cleaning, heat-insulating, and highly efficient microwave absorbing material. *Adv. Funct. Mater.* **2019**, *29*, 1807624.

[29] Wang, Y. C.; Yao, L. H.; Zheng, Q.; Cao, M. S. Graphene-wrapped multiloculated nickel ferrite: A highly efficient electromagnetic attenuation material for microwave absorbing and green shielding. *Nano Res.* **2022**, *15*, 6751–6760.

[30] Cheng, H. R.; Pan, Y. M.; Li, W.; Liu, C. T.; Shen, C. Y.; Liu, X. H.; Pan, C. F. Facile design of multifunctional melamine foam with Ni-anchored reduced graphene oxide/MXene as highly efficient microwave absorber. *Nano Today* **2023**, *52*, 101958.

[31] Fan, Q. W.; Song, C. Y.; Fu, P. Regulating N-doping strategies to construct 3D interconnected abundant porous N-doped carbon for polarization loss-enhanced microwave absorbers: Theory, design, and experiments. *J. Clean. Prod.* **2024**, *434*, 140118.

[32] He, J.; Liu, X. Y.; Deng, Y. H.; Peng, Y. H.; Deng, L. W.; Luo, H.; Cheng, C. P.; Yan, S. Q. Improved magnetic loss and impedance matching of the FeNi-decorated $Ti_3C_2T_x$ MXene composite toward the broadband microwave absorption performance. *J. Alloy. Compd.* **2021**, *862*, 158684.

[33] Qiu, J. F.; Liu, X.; Peng, C. Y.; Wang, S. H.; Wang, R. C.; Wang, W. Porous metal microsphere M@C-rGO (metal = Mn, Fe, Co, Ni, Cu) aerogels with high low-frequency microwave absorption, strong thermal insulation and superior anticorrosion performance. *J. Mater. Chem. A* **2024**, *12*, 21997–22012.

[34] Wang, S. H.; Liu, X.; Juan, Y.; Li, J. Y.; Zhang, T. Y.; Wang, W. Construction of mutifunctional Cu sphere@ZIF-derived Co particle/carbon fiber composites for high-efficiency microwave absorption. *Nano Res.* **2026**, *19*, 94908309.

[35] Pan, F.; Cai, L.; Shi, Y. Y.; Dong, Y. Y.; Zhu, X. J.; Cheng, J.; Jiang, H. J.; Wang, X.; Zhong, S.; Lu, W. Phase engineering reinforced multiple loss network in apple tree-like liquid metal/Ni–Ni_3P/N-doped carbon fiber composites for high-performance microwave absorption. *Chem. Eng. J.* **2022**, *435*, 135009.

[36] Cui, Y. H.; Yang, K.; Wang, J. Q.; Shah, T.; Zhang, Q. Y.; Zhang, B. L. Preparation of pleated RGO/MXene/Fe_3O_4 microsphere and its absorption properties for electromagnetic wave. *Carbon* **2021**, *172*, 1–14.

[37] Dong, H. Y.; Zhang, Y. H.; Yu, C.; Wang, Z. C.; Huang, Y. X. Eco-friendly microwave absorption metastructure: Design, optimization, and performance of CPVM based on PLA@CF. *Chem. Eng. J.* **2024**, 493.

[38] Shi, S. H.; Mou, P. P.; Wang, D.; Li, X. Y.; Teng, S. J.; Zhou, M. F.; Yu, X. L.; Deng, Z.; Wan, G. P.; Wang, G. Z. Co/carbon nanofiber with adjustable size and content of Co nanoparticles for tunable microwave absorption and thermal conductivity. *J. Materiomics.* **2024**, *10*, 124–133.

[39] Liu, S. J.; Wang, J.; Zhang, B.; Su, X. G.; Chen, X.; Chen, Y. H.; Yang, H.; Wu, Q. L.; Yang, S. Transformation of traditional carbon fibers from microwaves reflection to efficient absorption via carbon fiber microstructure modulation. *Carbon* **2024**, *219*, 118802.

[40] Gu, W. H.; Tan, J. W.; Chen, J. B.; Zhang, Z.; Zhao, Y.; Yu, J. W.; Ji, G. B. Multifunctional bulk hybrid foam for infrared stealth, thermal insulation, and microwave absorption. *ACS Appl. Mater. Interfaces* **2020**, *12*, 28727–28737.

[41] Zhang, X. P.; Wang, Q. Y.; Tang, Y. N.; Fan, G. H.; Hao, C. C.; Liu, Y. Decoration of conjugated polyacene quinone radical (PAQR) with Fe_3O_4 nanospheres achieving improved impedance matching and electromagnetic wave absorption. *Mater. Today Phys.* **2024**, *41*, 101349.

[42] Qiao, M. T.; Lei, X. F.; Ma, Y.; Tian, L. D.; He, X. W.; Su, K. H.; Zhang, Q. Y. Application of yolk-shell Fe_3O_4@N-doped carbon nanochains as highly effective microwave-absorption material. *Nano Res.* **2018**, *11*, 1500–1519.